(Received 30 March 2026, Accepted 13 May 2026, Scheduled 26 May 2026)

CMA-Based Flexible Four-Element SWB MIMO Antenna with Enhanced Isolation for Wearable Applications

Xiaoyan Wei[1], Zhonggen Wang[1], Wenyan Nie[2,*], Chenlu Li[3], and Zhengting Zhang[1]

[1] *School of Electrical and Information Engineering, Anhui University of Science and Technology, Huainan 232001, China*
[2] *School of Mechanical and Electrical Engineering, Huainan Normal University, Huainan 232001, China*
[3] *School of Electrical and Information Engineering, Hefei Normal University, Hefei 230061, China*

ABSTRACT: This paper proposes a flexible four-element super-wideband (SWB) multiple-input multiple-output (MIMO) antenna based on characteristic mode analysis (CMA) for wearable wireless communication, broadband sensing, and wireless body area network (WBAN) applications. The antenna employs a spiral mesh radiator combined with a defected ground plane incorporating triangular and T-shaped slots to form a multi-slot-coupled current path, enabling the cooperative excitation of multiple characteristic modes. The proposed antenna achieves an impedance bandwidth of 3.23–44.68 GHz, satisfying the SWB criterion. A four-port MIMO configuration is adopted to enhance diversity and isolation performance. Measured results agree well with simulations, with port isolation better than 20 dB across the operating band. In addition, the envelope correlation coefficient (ECC) is below 0.0015; the diversity gain (DG) is close to 10 dB; the total active reflection coefficient (TARC) is below −10 dB; and the channel capacity loss CCL) is less than 0.12 bit/s/Hz. The antenna also maintains stable SWB impedance matching and radiation performance under bending conditions, making it suitable for flexible SWB wearable and WBAN systems.

1. INTRODUCTION

With the rapid development of modern wireless communications, radar detection, microwave imaging, medical monitoring, and satellite systems, antennas capable of covering ultra-wide frequency spectra have become essential components in a wide range of applications [1, 2]. In particular, the 3–40 GHz frequency band encompasses 5G Sub-6 GHz and lower cellular communication systems, millimeter-wave bands, and multiple radar and sensing frequencies, and has emerged as a critical spectral resource for both current and next-generation wireless technologies [3, 4]. To satisfy the increasingly diverse requirements for frequency coverage, ultra-wideband (UWB) and super-wideband (SWB) antennas have attracted growing research interest. An SWB antenna is generally defined as a structure with a bandwidth ratio exceeding 10:1 [5]. However, achieving stable impedance matching and efficient radiation over such an extremely wide frequency range remains a challenging task, requiring careful structural design and a thorough understanding of the underlying electromagnetic mechanisms.

Meanwhile, flexible and wearable wireless systems have shown steadily increasing demand in applications such as human health monitoring, wireless body area networks (WBANs), and portable sensing devices [6–10]. Owing to their conformal capability, wideband transmission characteristics, and potential biocompatibility, flexible UWB antennas have become key enabling components in wearable medical devices, the flexible Internet of Things (IoT), and body-centric communication systems. Nevertheless, while satisfying structural requirements, including a low profile, lightweight construction, bendability, and conformality to complex surfaces, structural flexibility inevitably introduces additional electromagnetic uncertainties [11]. Specifically, physical deformation alters the effective permittivity and geometric boundary conditions, which inevitably result in impedance mismatch under bending conditions, radiation pattern distortion, and degradation in characteristic mode stability [12–16]. In this context, "characteristic mode stability" denotes the robustness of modal eigenvalues and surface current distributions against mechanical deformation. Its degradation indicates that bending-induced modal detuning or current redistribution directly compromises impedance matching and radiation performance. Most existing flexible UWB antenna designs rely on empirical bandwidth-enhancement techniques, such as slot loading [17], tapered geometries, or defected ground structures (DGSs) [18]. Although these approaches can achieve wide impedance bandwidths to a certain extent, they typically depend on extensive parameter sweeps and trial-and-error optimization, and lack a systematic physical explanation of the intrinsic coupling mechanisms among flexible-substrate dielectric properties, geometric deformation, and multimode radiation behavior. This limitation reduces the design predictability and performance robustness under variable bending conditions [19, 20].

To address these critical limitations, characteristic mode analysis (CMA) provides a rigorous eigenmode-based electromagnetic framework for revealing the intrinsic resonant behavior of conducting structures. By decomposing the total current into orthogonal characteristic modes, CMA offers valuable physical insight into the modal-evolution mechanisms as-

* Corresponding author: Wenyan Nie (wynie5240@163.com).

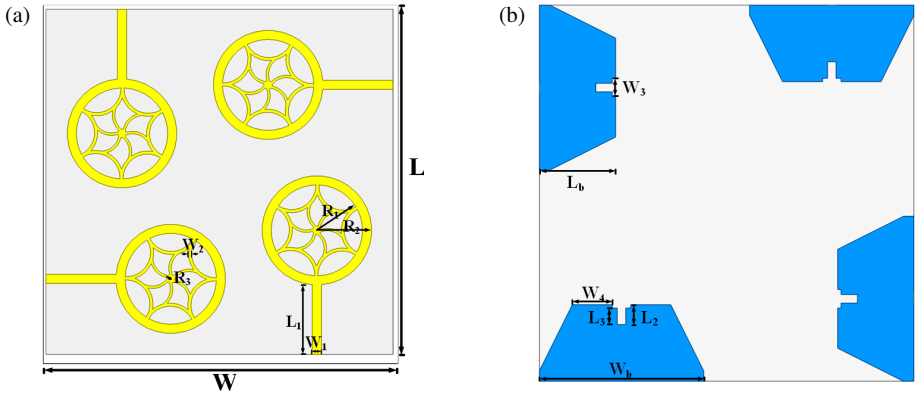

FIGURE 1. Geometry of the four-port MIMO antenna: (a) top view; (b) bottom view.

sociated with geometric modification and slot perturbation. This capability helps explain how multimode excitation contributes to the formation of SWB radiation characteristics and supports the bandwidth-enhancement strategy adopted in this work. Recent studies have demonstrated that CMA-assisted structural optimization of radiating elements and ground configurations can support stable excitation of multiple characteristic modes across wide frequency ranges in flexible UWB and multiple-input multiple-output (MIMO) antennas, thereby improving bandwidth stability, radiation efficiency, and port isolation under bending conditions. For example, a textile wearable antenna with a defected ground structure was optimized using CMA to enhance bandwidth for WBAN applications, and its on-body performance was further evaluated through specific absorption rate (SAR) analysis [19]. In the context of UWB MIMO antennas, a compact two-port UWB MIMO antenna using a unique DGS was analyzed by CMA to clarify the significant modes and their contributions to radiation while achieving improved inter-element isolation [20]. Furthermore, a miniaturized 4×4 UWB MIMO antenna with orthogonally arranged elements was designed and experimentally verified using CMA, demonstrating the usefulness of modal analysis for improving isolation and explaining the operating mechanism of multi-port UWB MIMO antennas [21]. Despite these advances, the systematic application of CMA to flexible wideband antennas, particularly for achieving the simultaneous excitation of both low-order and high-order characteristic modes over extremely wide frequency spans in SWB configurations, remains relatively limited.

Motivated by these considerations, this paper proposes a CMA-guided design methodology for a flexible four-element SWB MIMO antenna operating from 3.23 to 44.68 GHz. Unlike conventional empirical bandwidth-enhancement techniques that rely mainly on parameter tuning, the proposed approach systematically regulates the modal evolution of both the radiating element and the defected ground plane to construct a continuous multi-slot-coupled current path that supports the cooperative excitation of low-order and high-order characteristic modes across an extremely wide spectral range. In addition, the proposed spiral mesh radiator introduces distributed multiscale current paths that enhance modal-coupling capability and improve the excitation efficiency of higher-order characteristic modes at millimeter-wave frequencies. By combining CMA-assisted modal regulation with structural flexibility, the proposed antenna simultaneously achieves stable SWB impedance matching, high port isolation, and deformation robustness, thereby providing a practical design framework for next-generation wearable broadband communication and sensing-oriented MIMO systems.

2. ANTENNA DESIGN

2.1. Antenna Structure

The geometry of the designed flexible SWB antenna is shown in Fig. 1. It employs a Rogers Duroid 5880 substrate with a relative permittivity of $\varepsilon_r = 2.2$, a loss tangent of $\tan\delta = 0.0009$, and a thickness of 0.508 mm. At this ultra-thin thickness, the substrate exhibits excellent conformal capability, allowing it to adapt to moderate bending radii typically required in flexible wearable applications. It should be noted that Rogers 5880 is primarily chosen for design validation due to its stable dielectric properties and ultra-low loss across the entire 3.23–44.68 GHz band, which ensures the reliable characterization of the proposed CMA-based modal regulation methodology. This ultra-thin substrate provides a practical balance between conformability and structural stability under moderate bending conditions, making it suitable for proof-of-concept wearable prototypes, such as wrist-worn monitoring terminals, back-of-hand smart glove systems, or torso-worn WBAN gateway devices. The radiating element is composed of multiple symmetrically distributed spiral mesh structures. The design of these spiral elements ensures good radiation performance over the entire operating band and effectively broadens the bandwidth to meet the requirements of SWB communications. The radiating element adopts an optimized multi-arm symmetric spiral mesh

TABLE 1. Optimized parametric dimensions of the proposed MIMO antenna.

Parameters	L	L_1	L_2	L_3	L_b	W	W_1
Value (mm)	56	12	5.3	2.5	11.6	56	1.5
Parameters	W_2	W_3	W_4	W_b	R_1	R_2	R_3
Value (mm)	0.3	2.8	5	25	7.5	9	0.5

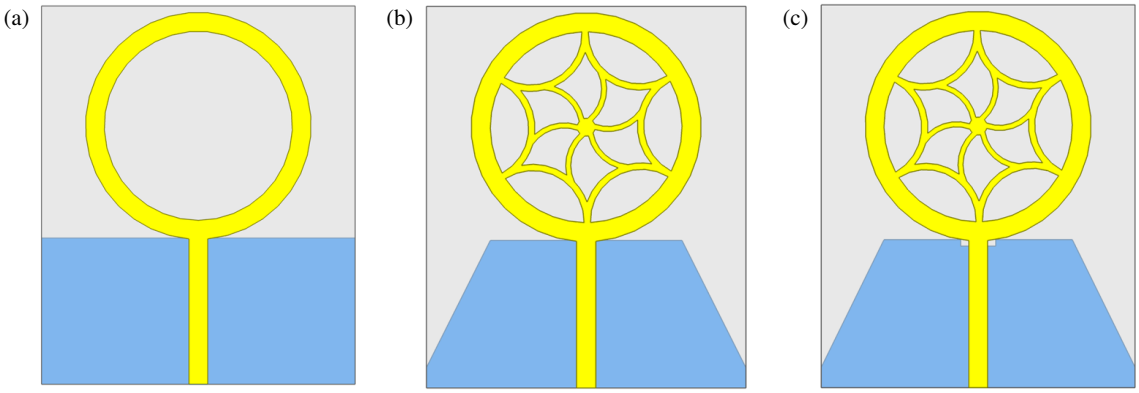

FIGURE 2. Structural evolution of a single antenna: (a) Antenna 1, (b) Antenna 2, (c) Antenna 3.

structure, which improves the radiation characteristics of the antenna. A rectangular ground plane is located on the bottom of the substrate, in which a T-shaped slot and two triangular slots are etched to further expand the bandwidth and reduce coupling. Due to the good impedance-matching performance and the inherent decoupling effect of the multi-slot DGS, no additional dedicated isolation structures are required. The optimized antenna parameters are listed in Table 1.

2.2. Design and Analysis of a Single Antenna Based on Characteristic Mode

To deeply understand the operating principle and systematically optimize the SWB performance of the proposed structure, CMA is utilized. For a conventional narrow-band circular ring radiator, the fundamental resonant frequency can be approximated by the analytical formula $f_c = c/(2\pi a\sqrt{\varepsilon_{eff}})$, where a is the mean radius, and ε_{eff} is the effective dielectric constant. However, this empirical equation is only applicable to the primary resonant mode. It is entirely insufficient for analyzing an SWB antenna that spans a massive 10:1 bandwidth ratio and relies on the cooperative excitation of multiple high-order modes. Therefore, CMA is strictly required as it provides a comprehensive mathematical modeling and modal-regulation design procedure. Based on the Method of Moments (MoM), CMA solves the generalized eigenvalue equation $[X]J_n = \lambda_n[R]J_n$, offering physical insights into the inherent resonant characteristics independent of any specific excitation. The extracted modes (e.g., Mode 2, 5, 7, ...) are true characteristic modes, each corresponding to a distinct eigenvalue λ_n and orthogonal eigencurrent. By extracting these orthogonal characteristic modes, the CMA systematically guided the core optimization of the proposed antenna in three critical aspects: identifying the optimal feed location via modal matching, extending the impedance bandwidth through continuous high-order mode excitation, and regulating the radiation patterns via the DGS. The effectiveness of the CMA-guided optimization is verified through the following structural evolution, reflection-coefficient comparison, modal significance, characteristic angle, and modal current distribution analyses.

The structural evolution of the proposed single antenna is illustrated in Fig. 2, and the corresponding simulated reflection

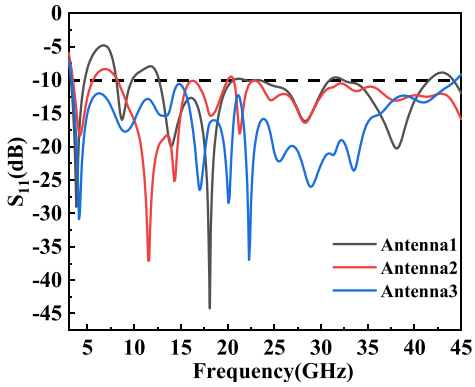

FIGURE 3. Simulated S-parameter plot of the antenna.

coefficients are presented in Fig. 3. The substrate size of the antenna is $30 \times 25 \times 0.508\,\text{mm}^3$. CMA was conducted in Computer Simulation Technology (CST) to investigate the modal-evolution behavior during the design process and to clarify the mechanism responsible for bandwidth enhancement.

The modal significance (MS) and characteristic angle (CA) of Antenna 1 are shown in Fig. 4, and the corresponding modal current distributions are presented in Fig. 5. It is worth noting that the characteristic modes extracted by the solver are inherently orthogonal. This orthogonality is algorithmically guaranteed by the eigenvalue decomposition process and can be physically verified via the distinctly non-overlapping spatial current distributions of different modes. MS describes the excitation capability of each mode within a specific frequency range, where values close to unity indicate strong modal resonance, whereas values below 0.707 correspond to weakly excited modes. CA further reflects the resonance condition of each mode, with values approaching 180°, indicating effective modal excitation. As observed in Fig. 5, Modes 2, 5, 7, and 11 exhibit relatively strong current concentration near the feeding region and circular patch structure, indicating their dominant contribution to radiation at this stage. However, higher-order Modes 14 and 15 remain weakly excited and are mainly distributed along the ground-plane edges, resulting in limited participation in broadband radiation. Consequently, the achievable impedance bandwidth of Antenna 1 cannot cover the target SWB operating band.

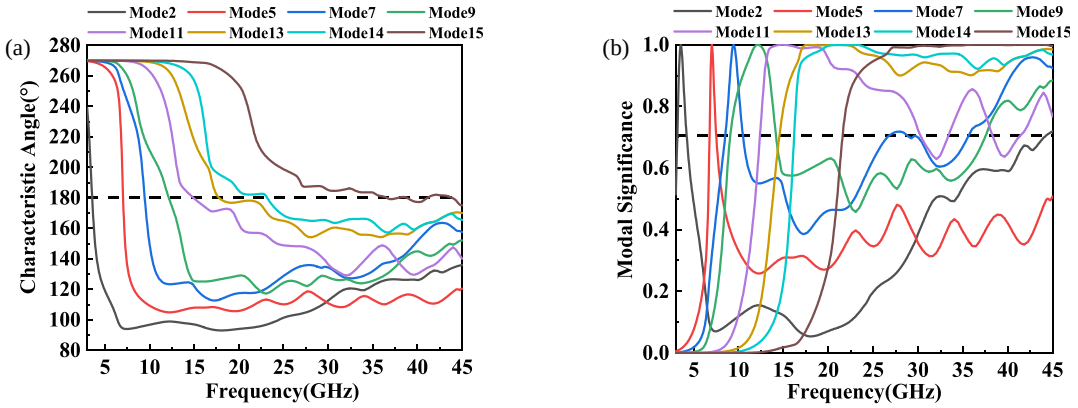

FIGURE 4. Simulated results of the mode analysis of Antenna 1: (a) CA, (b) MS.

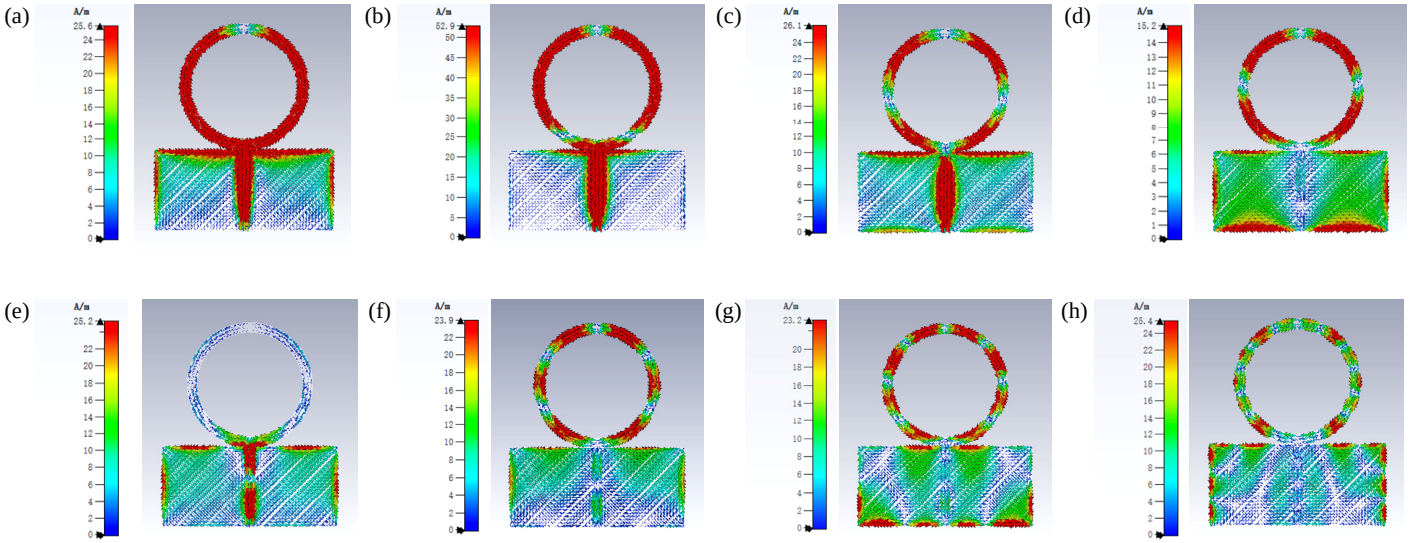

FIGURE 5. Simulated mode current distribution of Antenna 1: (a) Mode 2 at 3.56 GHz, (b) Mode 5 at 7.01 GHz, (c) Mode 7 at 9.44 GHz, (d) Mode 9 at 12.13 GHz, (e) Mode 11 at 14.91 GHz, (f) Mode 13 at 17.76 GHz, (g) Mode 14 at 23.18 GHz, (h) Mode 15 at 36.57 GHz.

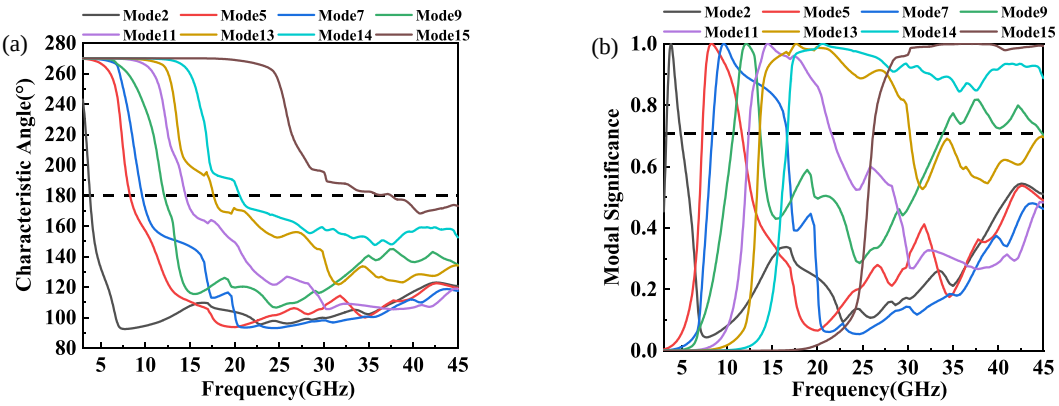

FIGURE 6. Simulated results of the mode analysis of Antenna 2: (a) CA; (b) MS.

To improve the modal-excitation capability, an additional spiral mesh radiator and two triangular slots are introduced to form Antenna 2, as shown in Fig. 2(b). The corresponding modal characteristics are presented in Figs. 6 and 7. Compared with Antenna 1, the spiral mesh structure effectively modifies the surface-current paths and enhances the excitation of multiple characteristic modes, particularly Modes 9 and 13 near the feeding region. Meanwhile, the triangular slots further regulate the current distribution on the ground plane and improve the coupling between the radiating patch and the ground structure. As a result, the combined excitation of Modes 2, 5, 7, 9, 11, and 13 contributes to a significantly broadened operating

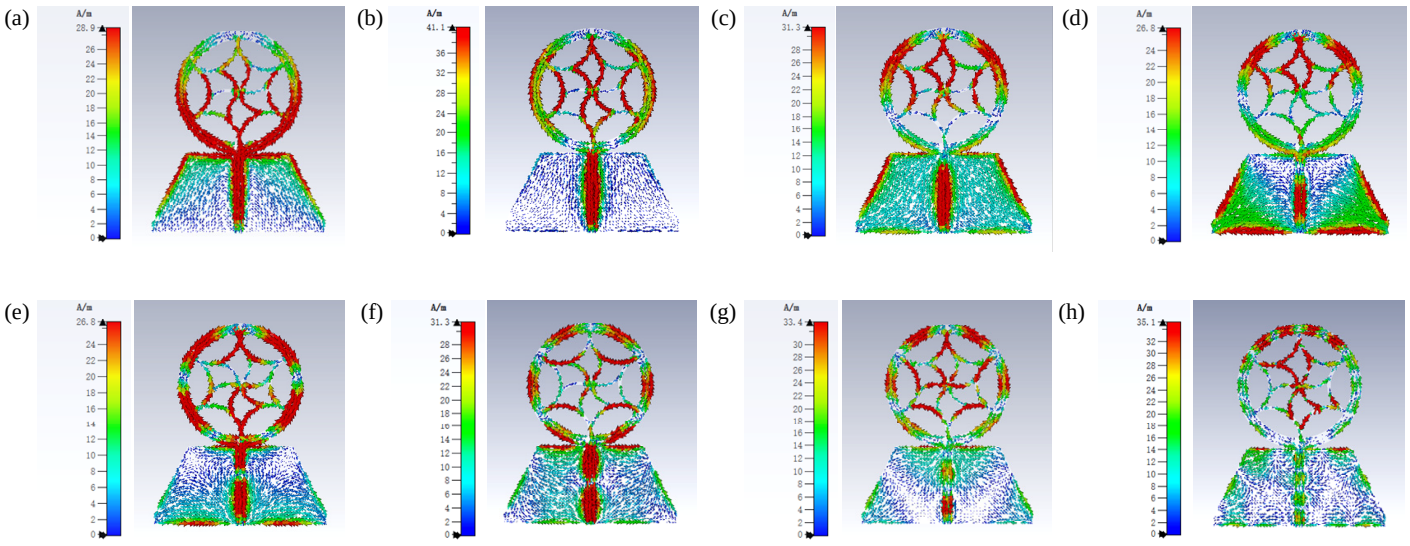

FIGURE 7. Simulated mode current distribution of Antenna 2: (a) Mode 2 at 3.77 GHz, (b) Mode 5 at 8.27 GHz, (c) Mode 7 at 9.65 GHz, (d) Mode 9 at 12.13 GHz, (e) Mode 11 at 14.48 GHz, (f) Mode 13 at 17.63 GHz, (g) Mode 14 at 20.57 GHz, (h) Mode 15 at 37.54 GHz.

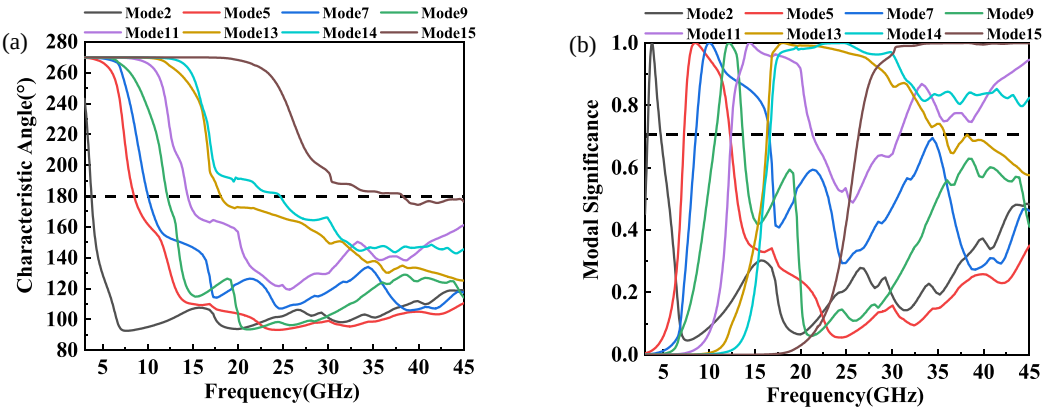

FIGURE 8. Simulated results of the mode analysis of Antenna 3: (a) CA, (b) MS.

bandwidth. Nevertheless, higher-order Modes 14 and 15 are still weakly excited, and the antenna bandwidth remains insufficient to satisfy the desired SWB bandwidth.

To further enhance the excitation efficiency of the higher-order modes and extend the operating bandwidth, a T-shaped slot is etched on the ground plane to form Antenna 3, as shown in Fig. 2(c). As demonstrated in Fig. 8, the MS of Mode 14 and Mode 15 shows a consistent improvement compared with Antenna 1 and Antenna 2, indicating stronger coupling between the feed line and these high-order modes. It should be noted that the S_{11} curves remain similar across the three designs because the fundamental and intermediate-order modes (Mode 2 to Mode 13) are already well matched in Antenna 1 and Antenna 2, and the T-shaped slot primarily affects the excitation of higher-order modes above 20 GHz. Since these high-order modes have negligible modal significance in the lower and middle frequency bands, their excitation enhancement has minimal impact on the overall S_{11} performance in these bands. The corresponding modal current distributions of Antenna 3 are illustrated in Fig. 9. Due to the synergistic interaction among the spiral mesh radiator, triangular slots, and T-shaped slot, a continuous multi-slot-coupled current path is established across both the patch and ground regions. This configuration effectively alters the boundary conditions and ground return paths. According to fundamental CMA theory, a mode is optimally excited when the feed aligns with its current maxima, which maximizes the modal excitation coefficient. The introduction of the multi-slot structure intentionally shifts the current maxima of higher-order modes toward the feeding region. As visually verified in Figs. 9(g) and 9(h), the intense current concentrations for Mode 14 (24.65 GHz) and Mode 15 (38.25 GHz) are now strongly localized around the feed and T-slot. This spatial modal matching enables the simultaneous and robust excitation of multiple characteristic modes, including the previously weakly excited higher-order Modes 14 and 15. In addition, the excitation levels of Modes 2, 5, 7, 9, 11, and 13 remain effective, resulting in improved multimode coupling across a wide frequency range. As confirmed by Fig. 8, these characteristic modes collectively cover the frequency range from 3.23 to 44.68 GHz, which agrees well with the simulated S_{11} parameters shown in Fig. 3 and verifies the effectiveness of the proposed modal-regulation strategy for achieving SWB operation.

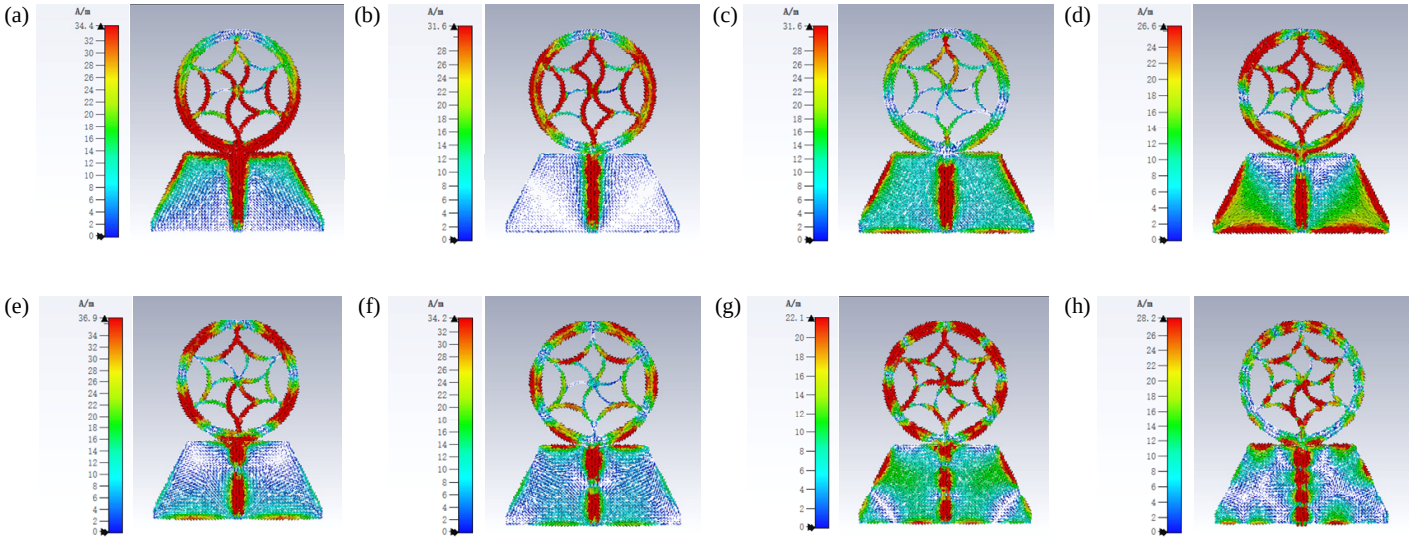

FIGURE 9. Simulated mode current distribution of Antenna 3: (a) Mode 2 at 3.77 GHz, (b) Mode 5 at 8.85 GHz, (c) Mode 7 at 10.03 GHz, (d) Mode 9 at 12.17 GHz, (e) Mode 11 at 14.44 GHz, (f) Mode 13 at 18.09 GHz, (g) Mode 14 at 24.65 GHz, (h) Mode 15 at 38.25 GHz.

It is worth noting that the CMA presented in Figs. 8 and 9 reveals that the narrow spiral mesh and ring composite structure adopted in this paper exhibits significant frequency-dependent radiation characteristics, and its SWB operation originates from the cooperative excitation of multi-order characteristic modes. In the lower frequency band of 3.23–6 GHz, the antenna has a moderate electrical size with a maximum aperture of approximately 0.75λ, where radiation is dominated primarily by the lowest-order characteristic mode (Mode 2), and the surface current forms clear standing-wave nodes and antinodes, typical of resonant-type radiation antennas that provide initial low-frequency coverage. In the middle frequency band of 6–20 GHz, as the electrical size becomes comparable to the operating wavelength, intermediate-order characteristic modes (Mode 5, 7, 9, 11, and 13) are sequentially excited with continuously overlapping modal significance curves, with Mode 5 extending smoothly from the lower band; their current distributions evolve gradually from standing-wave-dominant to a distributed propagating form, where currents in some regions of the spiral mesh exhibit progressive phase shifts while partial reflections persist at the spiral arm ends, forming a gradual transition region, where standing-wave and distributed-propagating characteristics coexist, and ensuring seamless continuity of impedance matching and radiation across the entire mid-band. In the upper frequency band of 20–44.68 GHz, the antenna becomes electrically large with an aperture size of approximately $8.2\lambda \times 8.2\lambda$. High-order characteristic modes (Mode 14 and 15) are strongly excited, with widely and uniformly distributed currents over the entire spiral mesh and no distinct standing-wave nodes or antinodes. Radiation in this regime arises from the constructive superposition of these high-order modes rather than ideal traveling-wave propagation, as the closed-loop spiral geometry inherently prevents pure traveling-wave behavior. Nevertheless, the CMA-guided design ensures efficient collective radiation with stable gain and no significant broadside pattern nulls.

The above analysis demonstrates that no single radiation mechanism dominates alone throughout the entire 3.23–44.68 GHz SWB operating range. Instead, the sequential and overlapping excitation of low-, intermediate-, and high-order characteristic modes achieved under the guidance of CMA provides a unified and physically rigorous explanation for the continuous SWB operation of this low-profile flexible antenna and also verifies the effectiveness of the CMA-based modal regulation method proposed in this paper.

2.3. MIMO Antenna Design and Analysis

To systematically investigate the influence of key structural parameters on the antenna's impedance matching and inter-element decoupling performance, a parametric sweep analysis of W_1 (width of the 50 Ω microstrip feed line) and W_4 (total horizontal length of the transverse arm of the T-shaped defected ground structure) was conducted. These two parameters were selected because W_1 is the core parameter affecting the equivalent current path and capacitive coupling at the feed port, and W_4 is the key parameter regulating the coupling current distribution on the defected ground plane. In the parametric sweep, only the target parameter was varied while all other structural parameters were kept constant, and the simulation results are presented in Fig. 10.

It can be observed that the variation of W_1 mainly affects the S_{11} parameter with a negligible influence on the isolation parameters S_{12}, S_{13}, and S_{14}. As W_1 increases, the equivalent capacitive coupling at the feed port is gradually optimized, leading to an improvement in the input impedance matching, a deeper resonance of S_{11}, and an expansion of the impedance bandwidth. However, when W_1 exceeds 1.5 mm, impedance overcompensation occurs at the feed port, which leads to the deterioration of S_{11} and a narrower bandwidth. This result indicates that W_1 regulates the resonant behavior of the antenna by modifying the equivalent current path and capacitive coupling

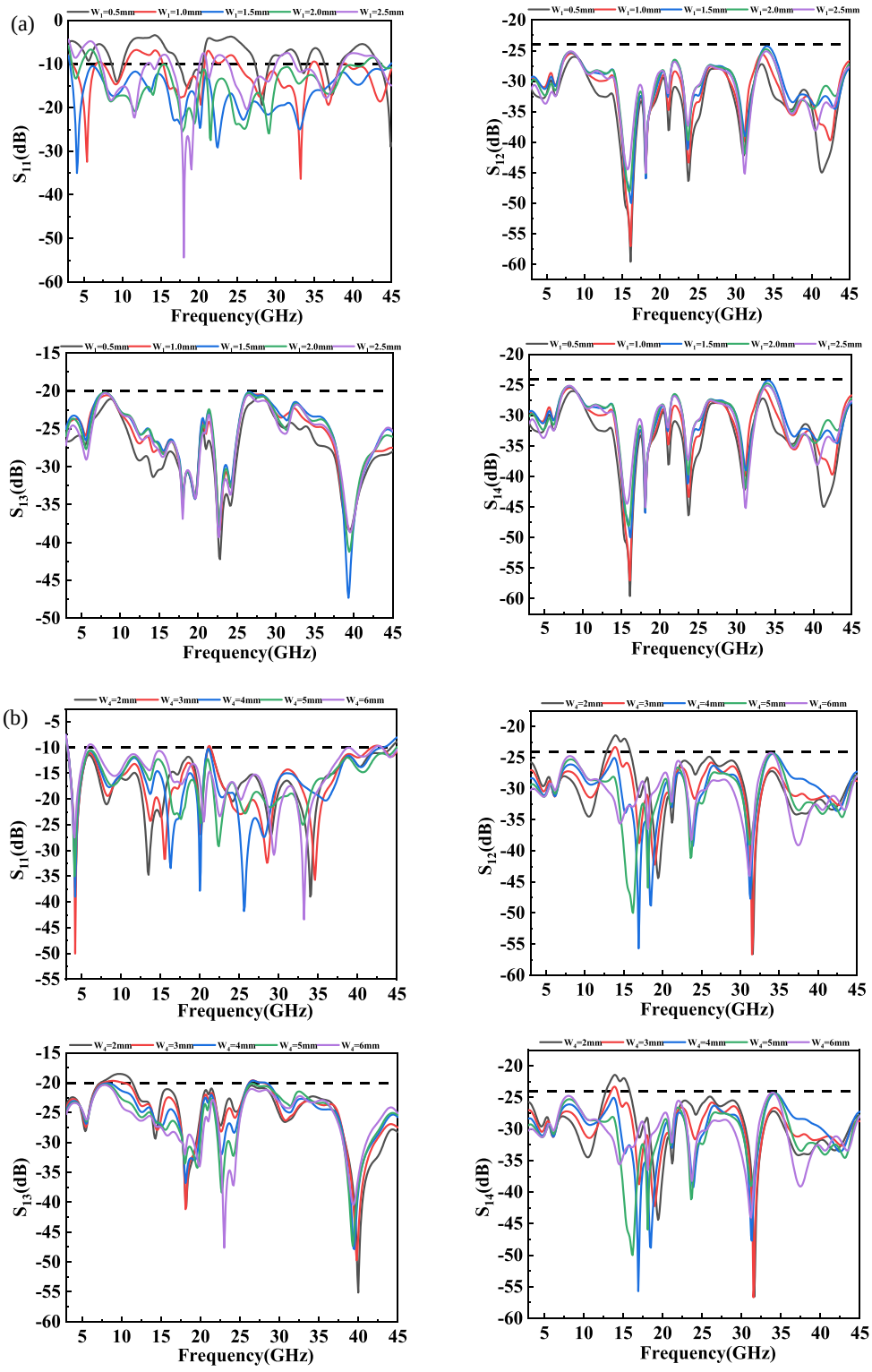

FIGURE 10. The effect of adjusted parameters on the simulated S-parameters of the antenna: (a) W_1, (b) W_4.

in the feeding region, thus optimizing the impedance matching performance of the antenna.

In contrast, as explicitly shown in the S_{11} plot of Fig. 10(b), when W_4 varies within the structural range of 2 mm to 6 mm, the fluctuation of S_{11} across the entire operating band is minimal (less than 2 dB difference). This quantitative stability indicates that the input impedance matching is highly robust to moderate variations in the horizontal length of the T-shaped DGS. Consequently, this allows W_4 to serve as an independent tuning variable for decoupling: it significantly affects the isolation parameter S_{12}. As W_4 increases, the coupling current distribution on the defected ground plane is effectively altered,

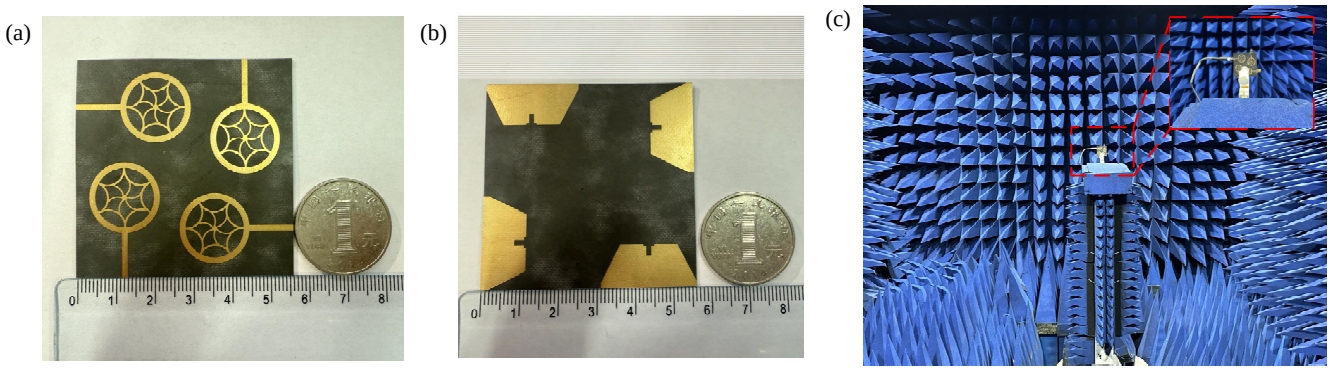

FIGURE 11. The proposed antenna fabricated prototype: (a) front view, (b) back view, (c) measurement environment.

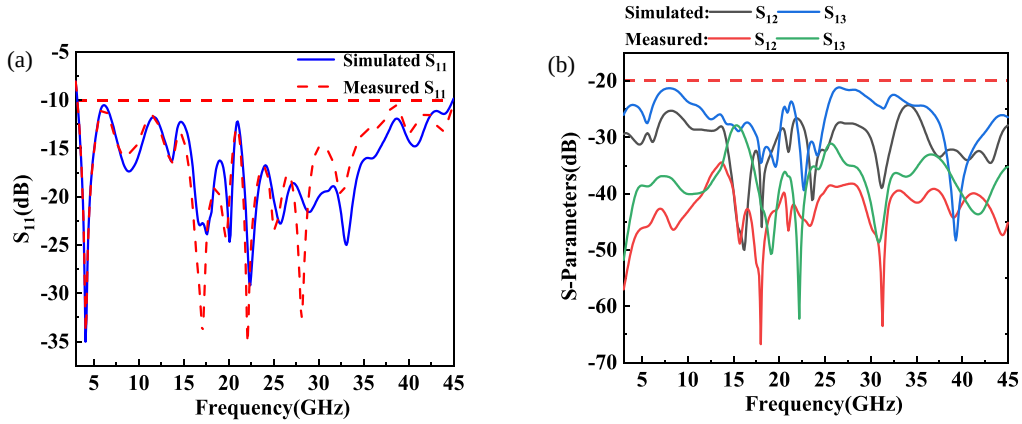

FIGURE 12. Simulated and measured S-parameters of the MIMO antenna: (a) S_{11}, (b) S_{12} and S_{13}.

and the equivalent coupling capacitance between antenna elements is reduced, leading to a progressive suppression of the mutual coupling and a noticeable reduction in S_{12} within the operating band. When W_4 exceeds 5 mm, the improvement in decoupling performance tends to saturate and even slightly degrade, because an excessively wide T-shaped slot disrupts the continuity of the ground plane current and introduces additional resonant modes. This result suggests that W_4 influences the energy transmission between ports by altering the coupling current distribution and equivalent coupling capacitance around the decoupling structure, thus effectively suppressing the inter-element mutual coupling.

In summary, W_1 and W_4 independently contribute to impedance matching and isolation enhancement, respectively. Through their coordinated optimization, the overall antenna performance is effectively improved. Considering both the impedance bandwidth and isolation characteristics, the optimal values of W_1 and W_4 are determined to be 1.5 mm and 5 mm, respectively.

3. RESULTS AND DISCUSSION

3.1. S-Parameters

The S-parameters of the antenna were measured using an Agilent N5235A vector network analyzer, and the measurement setup and physical prototype are shown in Fig. 11. Fig. 12 shows that the measured S_{11} results are in good agreement with simulated ones, covering the desired bandwidth of 3.23–44.68 GHz. In addition, S_{12} and S_{13} remain below -20 dB across the entire operating band, which indicates excellent isolation performance. Such excellent isolation performance benefits from the combined effects of a 90° rotationally symmetric orthogonal layout and multi-slot DGS. The orthogonal configuration introduces polarization diversity to weaken near-field mutual coupling between adjacent radiators. Meanwhile, the T-shaped and triangular slots etched on the ground plane act as current-restricting resonators to block surface current propagation. As analyzed from Fig. 12(b), the fluctuations and resonant dips in the S_{12} and S_{13} curves are closely associated with the resonance characteristics of DGS slots, which further suppress cross-port coupling current paths. In particular, the parametric optimization of W4 enables the DGS to achieve optimal decoupling in key frequency bands, ensuring stable isolation across the SWB range. Due to the 90° rotationally symmetrical arrangement of the four antenna elements, the isolation parameters between adjacent ports (e.g., S_{23}, S_{34}, and S_{41}) and diagonal ports (e.g., S_{24}) are essentially identical to S_{12} and S_{13}, respectively. Therefore, the presented results are representative of the overall inter-element decoupling performance. Minor discrepancies between the simulation and measurement results are mainly caused by fabrication and soldering errors, but the overall trends are consistent, confirming the stable performance of the antenna.

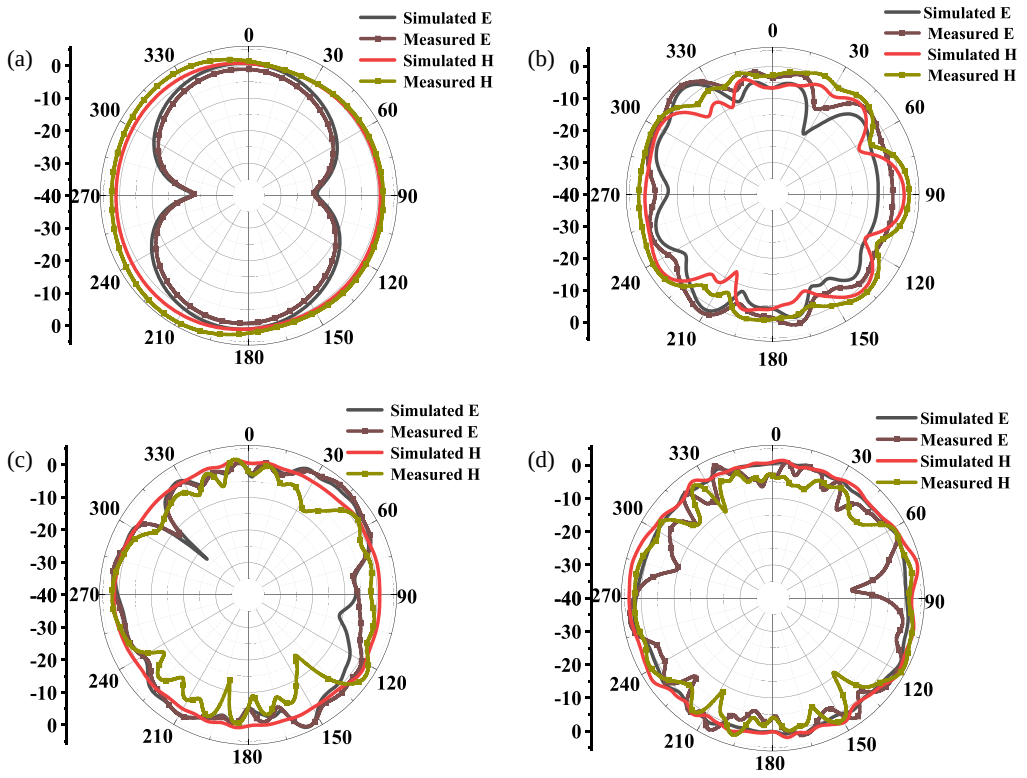

FIGURE 13. Simulated and measured radiation characteristics at (a) 4.1 GHz; (b) 22.4 GHz; (c) 33 GHz; and (d) 40.8 GHz.

3.2. Radiation Properties

The radiation properties of the proposed flexible MIMO antenna were characterized through simulation and measurement at 4.1, 22.4, 33, and 40.8 GHz, with the E-plane and H-plane radiation patterns presented in Fig. 13. At 4.1 GHz, the antenna exhibits a bidirectional radiation pattern in the E-plane and a quasi-omnidirectional distribution in the H-plane, which is consistent with the typical radiation behavior of a monopole-like resonator. At this frequency, the electrical size of the 56 mm $\times$ 56 mm radiator is approximately $0.75\lambda \times 0.75\lambda$, and the radiation is dominated by the lower-order resonant characteristic modes. As the operating frequency increases to 22.4, 33, and 40.8 GHz, the radiation patterns gradually evolve into more complex multilobed distributions. This behavior is a natural result of frequency-dependent pattern evolution rather than radiation instability. As the operating frequency enters the millimeter-wave region, the electrical size of the radiator increases significantly, reaching approximately $8.2\lambda \times 8.2\lambda$ at 40.8 GHz. Under such electrically large conditions, the cooperative excitation of multiple higher-order characteristic modes naturally leads to distributed multilobed radiation patterns. Although the radiation patterns become increasingly complex at higher frequencies, stable broadside radiation coverage is still maintained without significant radiation nulls in the boresight direction. In addition, the multilobed radiation characteristics at high frequencies can be beneficial for MIMO systems, since they provide enhanced spatial diversity and reduced multipath correlation in complex body-centric communication environments. The observed radiation behavior is also consistent with the distributed multi-mode radiation mechanism analyzed in Section 2.2.

As shown in Fig. 14, the peak realized gain increases from approximately 1.5 dBi at 4.1 GHz to approximately 8.8 dBi at 40.8 GHz, while the total efficiency (product of impedance matching efficiency and radiation efficiency) gradually improves from about 84% to 92% across the operating band. The realized gain can be approximated by $G_{dB} = 10\log_{10}(\eta) + D_{dB}$, where G is the realized gain, η the total efficiency, and D the directivity. Since the efficiency improvement from 84% to 92% corresponds to only about 0.4 dB, it cannot fully explain the observed 7.3 dB gain enhancement. Therefore, the directivity is also expected to increase with frequency.

At higher frequencies, the measured radiation patterns in Fig. 13 exhibit broader beam coverage in the H-plane together with increasingly pronounced multilobed characteristics. Although the broader H-plane beamwidth indicates reduced beam confinement in the azimuthal plane, the overall peak directivity depends on the three-dimensional radiation distribution rather than on a single radiation plane alone. In the E-plane, several narrower lobes appear at higher frequencies, leading to enhanced peak radiation intensity in specific directions. Based on the measured gain and efficiency, the estimated directivity increases from approximately 2.3 dBi at 4.1 GHz to approximately 9.2 dBi at 40.8 GHz. The increase in directivity is also consistent with the growth of the electrical aperture. The physical antenna size remains fixed at 56 mm $\times$ 56 mm, corresponding to approximately $0.75\lambda \times 0.75\lambda$ at 4.1 GHz and $8.2\lambda \times 8.2\lambda$ at 40.8 GHz. According to aperture radiation theory, $D \approx \eta_{ap} 4\pi A_{eff}/\lambda^2$, where A_{eff} is the effective aperture area, λ the free-space wavelength, and η_{ap} the aperture efficiency. As the operating frequency increases, the electrical aperture becomes significantly larger, naturally supporting higher directivity. The

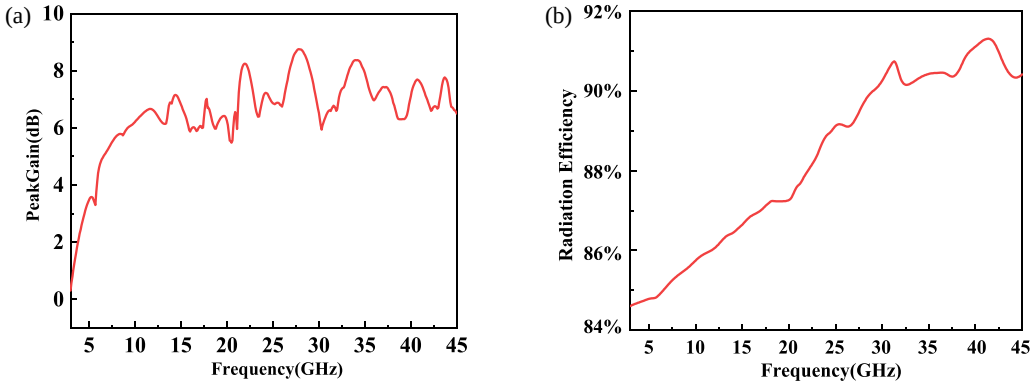

FIGURE 14. Peak realized gain and radiation efficiency: (a) Peak realized gain; (b) Radiation efficiency.

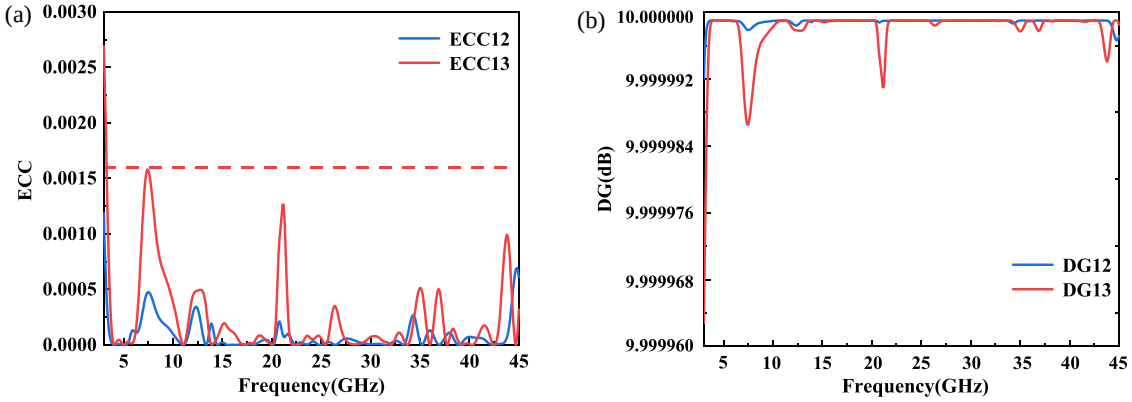

FIGURE 15. Simulated DG and ECC of the proposed antenna: (a) DG; (b) ECC.

measured directivity values are consistent with the nonuniform and multilobed field distributions caused by the cooperative excitation of multiple higher-order characteristic modes.

Furthermore, the low-loss Rogers Duroid 5880 substrate and defected ground structure help maintain high efficiency across the entire operating band. Even at the ultra-thin thickness of 0.508 mm, this low-loss characteristic effectively avoids severe energy attenuation at millimeter-wave frequencies, and similar high-gain performance with thin Rogers 5880 substrates has also been reported in [28]. At millimeter-wave frequencies, the spiral mesh radiator supports a more distributed aperture current distribution, which further contributes to the radiation performance enhancement.

Therefore, the gain enhancement originates from the combined effects of improved total efficiency and increased directivity associated with the enlarged electrical aperture and higher-order modal radiation. Overall, the measured and simulated radiation characteristics agree well, with minor discrepancies primarily attributed to fabrication tolerances and measurement uncertainties, thereby validating the stable SWB radiation performance of the proposed antenna.

3.3. MIMO Diversity Performance

3.3.1. DG and ECC

The diversity characteristics and mutual coupling performance of MIMO antennas are evaluated using the envelope correlation coefficient (ECC). ECC describes the correlation between the received signals of antenna elements and is calculated using (1), where lower values indicate better isolation. The diversity gain (DG), calculated from (2), reflects the diversity performance of the system. As shown in Fig. 15, the ECC of the proposed antenna remains below 0.0015 across the operating band, while the DG is close to 10 dB, indicating excellent diversity performance for communication applications in the 3.23–44.68 GHz band.

$$\mathrm{ECC}_{ij} = \frac{\left|S_{ii}^{*}S_{ij} + S_{ji}^{*}S_{jj}\right|^{2}}{\left(1-|S_{ii}|^{2}-|S_{ji}|^{2}\right)\left(1-|S_{jj}|^{2}-|S_{ij}|^{2}\right)} \quad (1)$$

$$\mathrm{DG} = 10 \times \sqrt{1-|\mathrm{ECC}|} \quad (2)$$

3.3.2. TARC and CCL

The total active reflection coefficient (TARC) is a key metric for evaluating the reflection performance of MIMO antennas. It comprehensively accounts for the reflected signals at the ports and the mutual coupling between elements and reflects the overall impedance-matching efficiency and port coupling by quantifying the total reflection characteristics of the system under all-port excitation. Ideally, TARC should remain below -10 dB, indicating efficient absorption of incident power and reduced reflection and mutual-coupling interference; it is calculated using (3). As shown in Fig. 16(a), the TARC of

TABLE 2. Performance comparison of the proposed MIMO antenna with other works.

Ref.	Substrate/Material	Size (mm^2)	Bandwidth (GHz)	Isolation (dB)	Peak Gain (dBi)	ECC	CMA
[22]	LCP	65×65	2.9–10.86	> 22	4.0	< 0.01	No
[23]	Jeans textile	21×16	3.35–4.12, 6.07–11.67	> 20.3	/	< 0.20	No
[24]	PDMS	56×41	3.4–11.8	> 20	4.3	< 0.02	No
[25]	PET	65×56	3.55–5.3	> 24	4.9	< 0.001	Yes
[26]	Flexible substrate	62×52	3.8–4.43, 5.25–6.3	> 23	5.2	< 0.02	Yes
[27]	Polyimide	57×50	3.6–3.8, 5.65–5.95	> 22	5.2/7.7	< 0.05	Yes
[28]	Rogers 5880	40×40	3.4–70	> 20	12	< 0.003	No
[29]	FR-4 + metal mesh	70×70	1.6–19.2	> 25	2.2–6.3	< 0.004	No
This work	**Rogers 5880**	$\mathbf{56 \times 56}$	**3.23–44.68**	$\mathbf{> 20}$	**2.0–8.8**	$\mathbf{< 0.0015}$	**Yes**

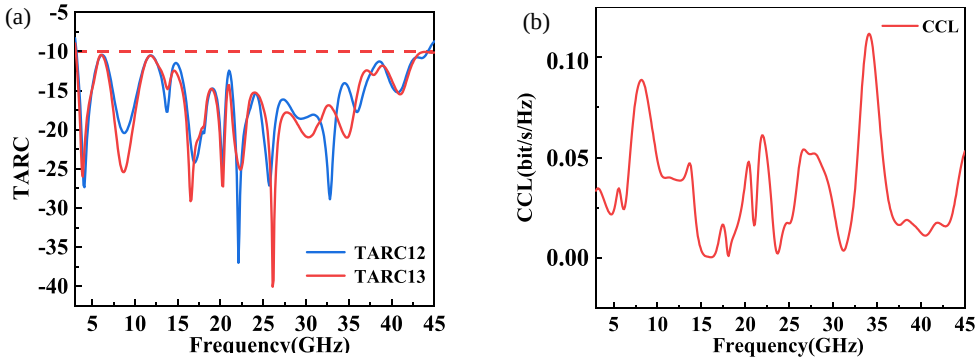

FIGURE 16. Simulated TARC and CCL of the proposed antenna: (a) TARC, (b) CCL.

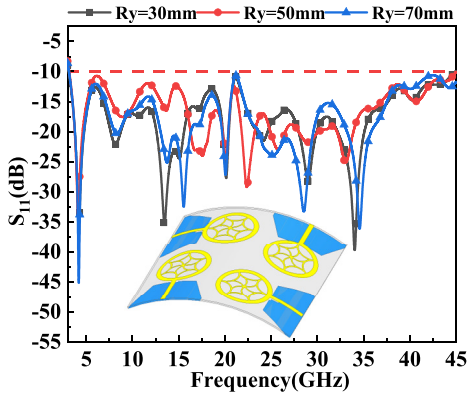

FIGURE 17. S_{11} parameters of the MIMO antenna under bending conditions.

the antenna remains below -10 dB across the 3.23–44.68 GHz band, demonstrating low inter-element mutual coupling and high channel independence, thereby enhancing the capacity of the MIMO system.

$$\mathrm{TARC} = \frac{\sqrt{\sum_{i=1}^{4}\left|S_{i1} + \sum_{n=2}^{4} S_{in}e^{j\theta n-1}\right|^2}}{2} \tag{3}$$

Channel capacity loss (CCL) is also an important parameter for evaluating MIMO antenna systems and is generally required to be less than 0.5 bit/s/Hz. It is calculated using (4)–(6), which involve the correlation matrix of the receiving antenna. Fig. 16(b) shows that the CCL of the proposed antenna is less than 0.12 bit/s/Hz, verifying the excellent performance of the MIMO antenna system.

$$\mathrm{CCL} = -\log_2(\Psi^R) \tag{4}$$

where Ψ^R denotes the receiver's correlation matrix, expressed as:

$$\Psi^R = \begin{bmatrix} \Psi_{11} & \Psi_{12} \\ \Psi_{21} & \Psi_{22} \end{bmatrix} \tag{5}$$

The elements of the matrix are defined as:

$$\begin{aligned} \Psi_{11} &= 1 - \left(|S_{12}|^2 + |S_{13}|^2\right) \\ \Psi_{12} &= -\left(S_{11} + S_{12} + S_{13} + S_{14}\right) \\ \Psi_{13} &= \left(S_{22} + S_{23} + S_{24} + S_{21}\right) \\ \Psi_{14} &= 1 - \left(|S_{21}|^2 + |S_{23}|^2\right) \end{aligned} \tag{6}$$

3.4. Bending Analysis and Numerical Simulation

To evaluate the bending performance of the antenna, the simulated S_{11} was analyzed for different bending radii along the y-direction, as shown in Fig. 17. Three bending radii ($Ry = 30$,

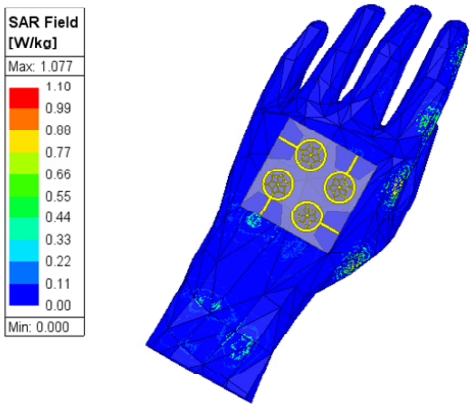

FIGURE 18. SAR analysis of the proposed antenna.

50, and 70 mm) were considered to examine the deformation tolerance of the proposed antenna, representing typical moderate bending conditions encountered in wearable applications, such as placement on the wrist, arm, and other curved body surfaces. As shown in Fig. 17, the resonant frequencies exhibit only slight variations with changes in the bending radius, indicating that the antenna maintains relatively stable electromagnetic characteristics under bent conditions. Meanwhile, the overall impedance bandwidth remains nearly unchanged, and the reflection coefficient stays below -10 dB over most of the operating band. These results indicate that the proposed MIMO antenna maintains stable impedance matching under mechanical deformation and shows good potential for applications in flexible wearable electronic devices.

3.5. Specific Absorption Rate

To evaluate the electromagnetic safety and suitability of the proposed flexible SWB MIMO antenna for wearable applications, a SAR analysis was performed. The antenna was simulated in close proximity to a high-fidelity hand phantom model in ANSYS HFSS. This investigation is crucial for ensuring that the radiation levels remain within the safety limits defined for human-tissue exposure during operation. The simulated SAR distribution, as illustrated in Fig. 18, indicates that the absorbed electromagnetic energy is primarily concentrated in the tissue regions directly adjacent to the antenna structure. Localized hot spots are observed near the antenna edges, which are attributed to near-field concentration under close-contact conditions. Most other parts of the hand model remain at a significantly lower exposure level, demonstrating that the electromagnetic interaction is spatially localized. Quantitatively, evaluated with a standard wearable reference input power of 0.1 W (20 dBm), the maximum simulated SAR value is 1.077 W/kg, averaged over 10 g of tissue. Despite the monopole-like structure exhibiting backward radiation in the far field, the near-field reactive energy is effectively distributed. The spiral mesh radiator diffuses the surface currents, preventing severe localized high-intensity E-field hotspots from penetrating the tissue. Consequently, this peak value is well below the safety limit of 2.0 W/kg mandated by the ICNIRP and IEEE C95.1. These results confirm that the proposed antenna satisfies the stringent SAR requirements for wearable devices across its super-wide operating band of 3.23–44.68 GHz. Consequently, the antenna is considered safe for practical use in flexible wearable systems and WBANs.

3.6. Comparative Study

To evaluate the proposed design, Table 2 provides a comparative performance analysis with SWB MIMO antennas. While flexible antennas in [22–24] and CMA-based designs [25–27] are primarily limited to the conventional UWB or Sub-12 GHz regions, [28] and [29] represent advanced SWB implementations, with [28] achieving a notable bandwidth up to 70 GHz. However, these wider-band designs typically lack the integration of structural flexibility or the systematic modal optimization provided by CMA. In contrast, the proposed four-port antenna achieves a continuous measured bandwidth of 3.23–44.68 GHz while maintaining good diversity metrics, including an isolation better than 20 dB and an ECC below 0.0015. By integrating the SWB radiation characteristics, CMA-guided design optimization, and favorable bending performance, the proposed scheme can provide a useful reference for future research in wearable wireless communications and broadband sensing.

4. CONCLUSION

A flexible four-element SWB MIMO antenna based on CMA is presented. A spiral mesh radiator combined with a defected ground plane incorporating triangular and T-shaped slots forms a multi-slot-coupled current path, enabling the cooperative excitation of multiple characteristic modes. The fabricated antenna achieves an impedance bandwidth of 3.23–44.68 GHz and excellent MIMO performance, with port isolation above 20 dB, ECC below 0.0015, DG close to 10 dB, TARC below -10 dB, and CCL less than 0.12 bit/s/Hz. The proposed antenna also exhibits stable performance under bending conditions. When the antenna is bent along the y-axis with different curvature radii, only slight variations in the resonant frequencies are observed. Meanwhile, the antenna maintains stable impedance matching across the SWB range, high isolation, and favorable radiation characteristics under bending conditions, thereby satisfying the conformal-bending requirements of wearable devices. Overall, the proposed antenna simultaneously achieves excellent SWB radiation performance, high isolation, strong diversity characteristics, and stable bending performance, providing a promising antenna solution for flexible wearable systems, broadband sensing, and next-generation wireless communication applications.

ACKNOWLEDGEMENT

This work was supported in part by the Natural Science Research Project of Anhui Educational Committee under Grant No. 2025AHGXZK31006, in part by the Research Foundation of Jiangsu Engineering Research Center for Bionics Control Technology and Equipment under No. FSKZ202503, and in part by the Anhui International Joint Research Center for Ancient Architecture Intellisencing and Multi-Dimensional Modeling under No. GJZZX2025KF03.

REFERENCES

[1] Yuan, X.-T., Z. Chen, T. Gu, and T. Yuan, "A wideband PIFA-pair-based MIMO antenna for 5G smartphones," *IEEE Antennas and Wireless Propagation Letters*, Vol. 20, No. 3, 371–375, 2021.

[2] Wu, B., X.-Y. Sun, H.-R. Zu, H.-H. Zhang, and T. Su, "Transparent ultrawideband halved coplanar Vivaldi antenna with metal mesh film," *IEEE Antennas and Wireless Propagation Letters*, Vol. 21, No. 12, 2532–2536, 2022.

[3] Li, J.-F., Q.-X. Chu, Z.-H. Li, and X.-X. Xia, "Compact dual band-notched UWB MIMO antenna with high isolation," *IEEE Transactions on Antennas and Propagation*, Vol. 61, No. 9, 4759–4766, 2013.

[4] Ren, J., W. Hu, Y. Yin, and R. Fan, "Compact printed MIMO antenna for UWB applications," *IEEE Antennas and Wireless Propagation Letters*, Vol. 13, 1517–1520, 2014.

[5] Dey, S. and N. C. Karmakar, "Design of novel super wide band antenna close to the fundamental dimension limit theory," *Scientific Reports*, Vol. 10, No. 1, 16306, 2020.

[6] Wong, K.-L., Y.-H. Hsu, C.-Y. Lee, and W.-Y. Li, "Wideband 4-port patch antenna module based compact 8-port two-module antenna for 6G upper mid-band 8×4 device MIMO with enhanced spectral efficiency," *IEEE Access*, Vol. 12, 88 976–88 991, 2024.

[7] Shabbir, T., R. Saleem, S. S. Al-Bawri, M. F. Shafique, and M. T. Islam, "Eight-port metamaterial loaded UWB-MIMO antenna system for 3D system-in-package applications," *IEEE Access*, Vol. 8, 106 982–106 992, 2020.

[8] Nie, L. Y., X. Q. Lin, S. Xiang, B. Wang, L. Xiao, and J. Y. Ye, "High-isolation two-port UWB antenna based on shared structure," *IEEE Transactions on Antennas and Propagation*, Vol. 68, No. 12, 8186–8191, 2020.

[9] Jayant, S. and G. Srivastava, "Close-packed quad-element triple-band-notched UWB MIMO antenna with upgrading capability," *IEEE Transactions on Antennas and Propagation*, Vol. 71, No. 1, 353–360, 2023.

[10] Chen, J., M. Wen, X. He, J. Xue, and X. Chen, "Compact, UWB, dual-polarized antenna based on tightly coupling effect," *IEEE Antennas and Wireless Propagation Letters*, Vol. 23, No. 10, 3292–3296, 2024.

[11] Pathak, P. A., S. L. Nalbalwar, A. E. Wagh, and J. L. Rajput, "A fractal approach to investigate SAR of HMSA UWB antenna for medical applications," *Progress In Electromagnetics Research C*, Vol. 154, 67–75, 2025.

[12] Wang, Z., H. Luo, J. Dong, M. Wang, J. Tong, C. Xiao, J. Zheng, and R. Wu, "Wearable broadband circularly polarized antenna with characteristic mode analysis for wireless body area network applications," *IEEE Antennas and Wireless Propagation Letters*, Vol. 24, No. 6, 1312–1316, Jun. 2025.

[13] Liu, A., J. Lu, P. K. Tan, and T. H. Gan, "Design of a low-profile dual-polarization wideband semi-flexible antenna," *IEEE Access*, Vol. 13, 5995–6005, 2025.

[14] Li, T., J. Gao, N. Rasool, M. A. Basit, and C. Chen, "Characteristic mode-based dual-mode dual-band of single-feed antenna for on-/off-body communication," *Electronics*, Vol. 13, No. 14, 2733, 2024.

[15] Ahmad, S., H. Boubakar, D. Segovia-Vargas, and T. A. Denidni, "A miniaturized CP antenna using superstrate for medical applications," *IEEE Open Journal of Antennas and Propagation*, Vol. 7, No. 2, 739–751, Apr. 2026.

[16] Hanif, M., M. Farhan, A. Sharif, M. Shahzad, N. Q. Soomro, K. N. Paracha, and U. Ijaz, "Characteristic mode analysis-based design and development of flexible UHF-RFID logo tag antenna for IoT wearable applications," *International Journal of Microwave and Wireless Technologies*, Vol. 17, No. 6, 1011–1018, 2025.

[17] Wu, B. and K.-M. Luk, "A UWB unidirectional antenna with dual-polarization," *IEEE Transactions on Antennas and Propagation*, Vol. 59, No. 11, 4033–4040, 2011.

[18] Yang, M., C. Liu, and X. Liu, "Design of π-shaped decoupling network for dual-polarized Y-probe antenna arrays," *IEEE Antennas and Wireless Propagation Letters*, Vol. 21, No. 6, 1129–1133, 2022.

[19] Elias, B. B. Q., P. J. Soh, A. A. Al-Hadi, P. Akkaraekthalin, and G. A. E. Vandenbosch, "Bandwidth optimization of a textile PIFA with DGS using characteristic mode analysis," *Sensors*, Vol. 21, No. 7, 2516, 2021.

[20] Kempanna, S. B., R. C. Biradar, P. Kumar, P. Kumar, S. Pathan, and T. Ali, "Characteristic-mode-analysis-based compact vase-shaped two-element UWB MIMO antenna using a unique DGS for wireless communication," *Journal of Sensor and Actuator Networks*, Vol. 12, No. 3, 47, 2023.

[21] Suresh, A. C. and T. S. Reddy, "Experimental investigation of novel frock-shaped miniaturized 4×4 UWB MIMO antenna using characteristic mode analysis," *Progress In Electromagnetics Research B*, Vol. 101, 45–61, 2023.

[22] Zhang, J., C. Du, and R. Wang, "Design of a four-port flexible UWB-MIMO antenna with high isolation for wearable and IoT applications," *Micromachines*, Vol. 13, No. 12, 2141, 2022.

[23] Biswas, A. K., B. Basu, and A. Nandi, "Compact wearable UWB MIMO antenna with reduced mutual coupling and notch characteristics of WLAN band," *Arabian Journal for Science and Engineering*, Vol. 47, No. 11, 14 561–14 569, 2022.

[24] Jhunjhunwala, V. K., P. Kumar, A. P. Parameswaran, P. R. Mane, O. P. Kumar, T. Ali, S. Pathan, S. Vincent, and P. Kumar, "A four port flexible UWB MIMO antenna with enhanced isolation for wearable applications," *Results in Engineering*, Vol. 24, 103147, 2024.

[25] John, D. M., S. Vincent, S. Pathan, and T. Ali, "Characteristics mode analysis based wideband sub-6 GHz flexible MIMO antenna using a unique hybrid decoupling structure for wearable applications," *Physica Scripta*, Vol. 99, No. 3, 035032, 2024.

[26] John, D. M., S. Vincent, K. Nayak, B. S. Supreetha, T. Ali, P. Kumar, and S. Pathan, "A compact flexible four-element dual-band antenna using a unique defective ground decoupling structure for sub-6 GHz wearable applications," *Results in Engineering*, Vol. 21, 101900, 2024.

[27] John, D. M., T. Ali, S. Vincent, S. Pathan, J. Anguera, B. Virdee, R. M. David, K. Nayak, and S. P. Gopi, "A dual-band flexible MIMO array antenna for sub-6 GHz 5G communications," *Sensors*, Vol. 25, No. 11, 3557, 2025.

[28] Esmail, B. A. F., S. Koziel, and A. Pietrenko-Dabrowska, "Design and optimization of a compact super-wideband MIMO antenna with high isolation and gain for 5G applications," *Electronics*, Vol. 12, No. 22, 4710, 2023.

[29] Yang, Z., J. Nan, J. Liu, Y. Wang, and X. Zhao, "A transparent MIMO antenna employing metal mesh structure for SWB," *IEICE Electronics Express*, Vol. 21, 20240339, 2024.